

Large Scale Structure Prediction of Near-Stoichiometric Magnesium Oxide Based on a Machine-Learned Interatomic Potential: Novel Crystalline Phases and Oxygen-Vacancy Ordering

Hossein Tahmasbi,¹ Stefan Goedecker,² and S. Alireza Ghasemi^{1,*}

¹*Department of Physics, Institute for Advanced Studies in Basic Sciences (IASBS), Zanjan 45137-66731, Iran*

²*Department of Physics, Universität Basel, Klingelbergstrasse 82, 4056 Basel, Switzerland*

(Dated: December 4, 2021)

Using a fast and accurate neural network potential we are able to systematically explore the energy landscape of large unit cells of bulk magnesium oxide with the minima hopping method. The potential is trained with a focus on the near-stoichiometric compositions, in particular on suboxides, i.e., $\text{Mg}_x\text{O}_{1-x}$ with $0.50 < x < 0.60$. Our extensive exploration demonstrates that for bulk stoichiometric compounds, there are several new low-energy rocksalt-like structures in which Mg atoms are octahedrally six-coordinated and form trigonal prismatic motifs with different stacking sequences. Furthermore, we find a dense spectrum of novel non-stoichiometric crystal phases of $\text{Mg}_x\text{O}_{1-x}$ for each composition of x . These structures are mostly similar to the rock salt structure with octahedral coordination and five-coordinated Mg atoms. Due to the removal of one oxygen atom, the energy landscape becomes more glass-like with oxygen-vacancy type structures that all lie very close to each other energetically. For the same number of magnesium and oxygen atoms our oxygen-deficient structures are lower in energy if the vacancies are aligned along lines or planes than rock salt structures with randomly distributed oxygen vacancies. We also found the putative global minima configurations for each composition of the non-stoichiometric suboxide structures. These structures are predominantly composed of (111) slabs of the rock salt structure which are terminated with Mg atoms at the top and bottom, and are stacked in different sequences along the z -direction. Like other Magnéli-type phases, these structures have properties that differ considerably from their stoichiometric counterparts such as low lattice thermal conductivity and high electrical conductivity.

I. INTRODUCTION

Magnesium oxide, one of the most abundant minerals in the lower mantle of the earth [1], has been the subject of many experimental and theoretical studies due to its importance in various industrial applications [2]. Furthermore, MgO has served as a prototypical system to evaluate the thermal conductivity of the deep mantle of the earth at high pressures and temperatures [3–5], and can be used as a catalyst for various chemical reactions [6–8]. In particular, MgO can support metal clusters in catalytic processes [9, 10], and MgO clusters are good candidates for hydrogen adsorption due to the polarity of the Mg–O bonds [11]. Also, MgO surfaces with strong polarity, e.g. MgO(111), can be employed as support in photocatalytic water splitting experiments [12].

Like some other binary solids such as sodium chloride and cadmium oxide, MgO crystallizes under ambient conditions in the cubic rock salt (RS) phase ($Fm\bar{3}m$), where the atoms are octahedrally coordinated. It has high thermal [13] and low electrical conductivity [14] with a large band gap of 7.83 eV. Previous theoretical studies suggest that there exists a dense spectrum of low-energy polymorphs for MgO, some of which have been discovered and reported in the literature [15, 16]. Therefore, the exploration of the potential energy landscape of MgO has attracted much attention in recent years [16–19]. Limpijumnon *et al.* [17] studied the transition between the wurtzite and RS phases of MgO and discovered the h -MgO polymorph with five-fold coordination. The five-coordinated structures of MgO, together with the lowest-energy structures

of ZnO and ZnS, have mainly been explored by Schön [18]. Zwijnenburg *et al.* [16] systematically mapped out the potential energy surfaces (PESs) of MgO using the basin hopping method in conjunction with an interatomic potential implemented in the GULP code [20]. They discovered low-density phases of MgO and found several new crystal structures with four-, five-, or six-coordinated Mg atoms which are relatively low in energy. Furthermore, the PES of MgO was explored by a novel approach which uses the random superlattice structure sampling [19] followed by local relaxations at the density functional theory (DFT) level. It resulted in the discovery of different polymorphs of several ionic systems, e.g. MgO, ZnO, and SnO_2 , and the experimental structures were found more frequently than the hypothetical structures. In fact, the surprising complexity of the PESs of binary solids that crystallize in octahedral structures at ambient conditions makes it difficult to explore in an exhaustive way the spectrum of possible structures.

Only little is known about the PESs of non-stoichiometric crystal phases of MgO (i.e. Mg_nO_m , $n \neq m$) since most of the previous studies have focused on the stoichiometric composition. However, many efforts have been made to better understand the defects at the bulk and the surface of MgO [21]. Among all the defects, the oxygen vacancy is the most important that can substantially change properties and the chemical behaviour of MgO structures [8, 22]. In addition, a few attempts have been made to study non-stoichiometric clusters of MgO [23, 24]. Such studies have demonstrated that non-stoichiometric clusters exhibit peculiar magnetic properties [25].

In recent years, neural network potentials (NNPs) [26, 27] have emerged to overcome computational limitations of density functional based approaches. Because of its reduced nu-

* aghasemi@iasbs.ac.ir

merical cost, this approach makes it possible to model the PESs of large systems with hundreds or even thousands of atoms. In this way new phenomena that can only be observed on larger length scales can be discovered. Vacancy ordering is such a phenomenon that will be investigated in this study. Neural network potentials have already been successfully constructed for different compounds and have been employed for crystal structure predictions [28–32], to discover 2D materials [33], to study gas-surface interactions [34], for the systematic investigations of surface reconstructions [35], etc.

In this work, we train a NNP to study the MgO system based on the Charge Equilibration via Neural network Technique (CENT) [27] as implemented in the FLAME code [36]. A more detailed description of CENT can be found elsewhere [27, 28, 36]. We demonstrate for the first time that the CENT method can also accurately reproduce the PES of non-stoichiometric systems that have a more complex potential energy surface. For this purpose, we train a highly transferable neural network potential for magnesium oxide for both stoichiometric and non-stoichiometric compositions of clusters and crystals. We show that this potential gives rise to accurate second and third-order interatomic force constants which allow us to compute dynamical properties that are in good agreement with DFT results.

We use this NNP to probe the energy landscape of bulk structures of MgO with a main focus on the suboxide near-stoichiometric compositions which are of fundamental importance. For the stoichiometric compounds, we find novel low-energy polymorphs for MgO in addition to recovering all the well-known structures in the literature. To represent these structures, large simulation cells containing up to 32 atoms are required. For the near-stoichiometric compositions of MgO, namely, $\text{Mg}_x\text{O}_{1-x}$ with $0.51 \leq x \leq 0.57$, we find many new polymorphs with similar structural features which mostly have small band gaps or pseudogaps due to the appearance of defect states in the gap. They are energetically more favorable than the classical defect structures of RS.

In addition, we find that the global minimum of all compositions have nearly identical structural motifs and symmetries. These structures are RS structures along the [111] direction in which a layer of oxygen atoms is removed. Therefore, they are composed of slabs which terminate with Mg atoms and only the number of their layers or the octahedral motifs changes with the number of atoms in their primitive cell. Unlike RS, these structures have metallic behaviour with low lattice thermal conductivity.

This manuscript is organized as follows. In Sec. II we describe the methods employed in this work including the training process of the CENT potential and its validation as well as our search method. Sec. III contains the results on the stoichiometric and non-stoichiometric bulk structures of MgO. Finally, the main conclusions are summarized in Sec. IV.

II. METHOD

A. Density functional theory

We employ two different software packages to perform the DFT calculations in this work. The training data for our CENT potential are generated using the *ab initio* molecular simulation package (FHI-aims) [37]. We use the PBE exchange-correlation functional [38] for both free and periodic boundary conditions with the default tight settings, i.e. tier 1 and tier 2 basis functions for Mg and O, respectively. The predicted structures from the NNP and their properties (e.g., geometry relaxation, phonon dispersions etc.) are refined using the projector augmented wave (PAW) formalism as implemented in the Vienna *ab initio* Simulation Package (VASP) [39–42]. A plane-wave cutoff energy of 550 eV and k-point mesh with a density of 0.03 \AA^{-1} were used to obtain converged results.

B. Neural network potential

1. Training

To probe the PESs of the near-stoichiometric compounds, we train an accurate artificial neural network (ANN) potential to model atomic interactions using the CENT method. Our ANN potential models the PESs of both stoichiometric and various non-stoichiometric MgO systems with the same parameter set. This is highly challenging since we have to accurately describe not only the configurational space but also the compositional space. For this purpose, the CENT potential has to be trained with a hierarchical approach, and a variety of different reference data sets are required.

To start the training process, we use NaCl-type structures which were obtained from Ref. [27] as the initial training data set by scaling the bond lengths to typical values for MgO. Also, we include the global minima (GM) structures of MgO clusters of different sizes (MgO_4 to MgO_{36}) which were found by Chen *et al.* [43]. As a result, we select more than 2200 diverse structures to train a CENT potential in the first step. The ANN architecture $70 - 5 - 5 - 1$ is employed, i.e., 70 symmetry functions, including 16 radial functions and 54 angular functions [44], with two hidden layers each containing 5 nodes, and one output layer. The output layer is taken as the electronegativity of the given atom where the input layer is fed with the symmetry functions as environment descriptors with a cutoff radius of 11 Bohr.

By combining this first, initially trained potential together with the minima hopping (MH) method (see Sec. II C), we perform a preliminary search on the high dimensional PES of $(\text{MgO})_n$ clusters with $n = 8, 11, 13, 14, 19, 26, 28$, and 40. After removing all similar and high energy structures by comparing the environment descriptors [27, 44] implemented in FLAME, we select more than 7100 stoichiometric neutral clusters with a large diversity. This filtering step is crucial to prevent overfitting. Using this data set, we then train in a sec-

ond step a CENT potential that can be applied to the stoichiometric bulk and cluster structures of MgO. Note that twenty percent of the data set is randomly selected as a validation set to monitor the performance of the training.

Using this second CENT potential, we explore the PES of stoichiometric clusters $(\text{MgO})_n$ ($n = 4 - 40$) and crystalline Mg_nO_n ($n = 2 - 48$) structures. We recover all GM structures which were previously reported for clusters of magnesium oxide [23, 43, 45, 46]. Further, we use this second potential to find several non-stoichiometric MgO structures, i.e., $\text{Mg}_x\text{O}_{1-x}$ for both clusters ($x = 0.53$ to $x = 0.60$) and bulk systems ($x = 0.55$ to $x = 0.57$) with different supercell sizes. In this way, we find a diverse set of non-stoichiometric structures although non-stoichiometric structures had not been included in the training data set.

In a third, final step, we expand the reference data set by adding all structures, both stoichiometric and non-stoichiometric, that we generate in step two to the training set. In total, we use 24180 structures as training data set including both stoichiometric and non-stoichiometric clusters and crystalline structures.

Note that in each step of the training process, we run the FLAME code several times with different initializations of both the CENT parameters (electronegativity offset, hardness, Gaussian widths) and neural network weights. The best parameter set for the final calculations is selected based on the root mean squared error (RMSE) values of energy and atomic forces as well as the size of the variations in charge and electronegativity. In the final training step, the RMSEs of energy and atomic forces are less than 11 meV/atom and 0.257 eV/Å, respectively. The parameters and weights of the trained potential for MgO are available in the FLAME code [36].

2. Validation

In order to examine the quality and reliability of the CENT potential, we employ it to calculate various (physical) properties. As a first test, we perform phonon calculations for the RS structure with the frozen phonon approach as implemented in the PHONOPY package [47]. A large supercell $5 \times 5 \times 5$ containing 250 atoms is used to ensure the convergence of the force constants and the phonon density of states (DOSs). Figure 1 compares the phonon dispersions calculated by DFT and CENT, showing good agreement in particular for the acoustic modes, which dominate the thermal transport properties. Since the optical branches have very small group velocities, they contribute little to the heat transport process [48, 49].

Next, we compute the lattice thermal conductivity of the RS phase of MgO, which requires also the third-order derivatives of the potential energy. We compute the second and third-order interatomic force constants (IFCs) with PHONOPY and thirdorder.py [50], respectively. The third-order IFCs are calculated with $5 \times 5 \times 5$ supercells, truncating the interactions beyond the sixth nearest neighbors. The IFCs are fed into the ShengBTE code [50] to iteratively solve the Boltzmann transport equation for phonons.

Figure 2 shows the lattice thermal conductivity of RS at

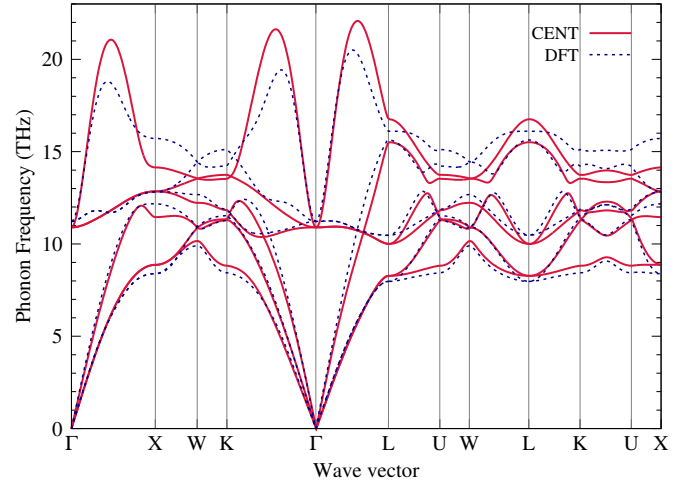


FIG. 1. Comparison of the phonon dispersion of the MgO rock salt obtained with DFT and CENT calculations. The LO-TO splitting was neglected.

different temperatures using DFT and CENT. The comparison shows good agreement between the DFT and CENT, with deviations between 5% and 7% at 300 K and 4000 K, respectively. Further, our results are in excellent agreement with the experimental and theoretical results in the literature [13, 51, 52].

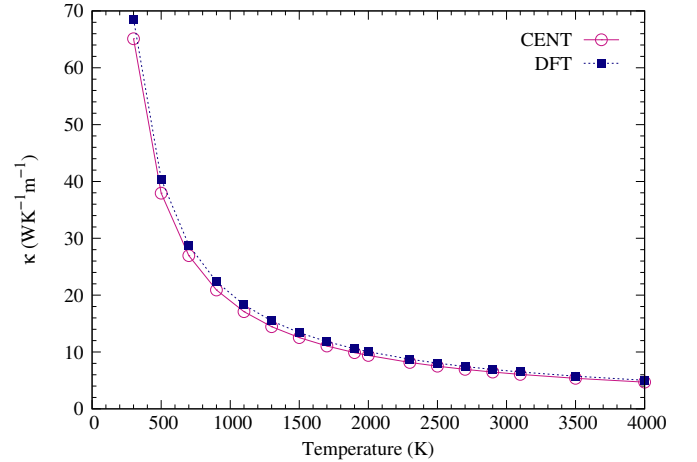


FIG. 2. Comparison of the DFT and CENT results for the thermal conductivity of the MgO rock salt at different temperatures.

Finally, we use the MH method to screen the PESs of both cluster and crystal structures with different sizes and stoichiometries. We validate that our CENT potential reproduces all results in the literature [16, 43, 53] as local minima on the PESs. Furthermore, we compare the energetics of the local minima from CENT with reference DFT values to ensure that the energetic ordering agree with each other in almost all cases. We also repeated the phonon calculations for several of the non-stoichiometric structures, and performed geometry relaxation for 100 stoichiometric and non-stoichiometric bulk structures to compare their energies with DFT values. Based

on these rigorous tests, we conclude that our ANN potential is sufficiently accurate to perform structure prediction as well as to accurately estimate the thermal properties of the MgO system.

C. Structural search

We explore the energy landscape of bulk phases of MgO in a systematic way using the minima hopping (MH) method [54–57] which is an efficient search approach for global optimization and is implemented in the FLAME code. We investigate stable phases of $\text{Mg}_x\text{O}_{1-x}$ with $x = 0.51$ to 0.57 , i.e., for the seven compositions Mg_4O_3 ($x = 0.57$), Mg_5O_4 ($x = 0.56$), Mg_6O_5 ($x = 0.55$), Mg_7O_6 ($x = 0.54$), Mg_8O_7 ($x = 0.53$), $\text{Mg}_{12}\text{O}_{11}$ ($x = 0.52$), and $\text{Mg}_{20}\text{O}_{19}$ ($x = 0.51$). Our simulation cells contain up to 22 f.u., i.e., supercells including 7 to 46 atoms.

Even though the stoichiometric bulk structures Mg_nO_n ($n = 4$ to 16 , $x = 0.50$) were originally intended only as a validation test, we discovered a plethora of new, low energy structures for these stoichiometric configurations when using larger unit cells. For each simulation cell size, we perform MH runs at least 20 times with different starting configurations to thoroughly scan the PES.

Selected structures are then refined at the DFT level. In this selection process, we first remove all structures with CENT energies higher than 300 meV/atom with respect to the minimum structure in each composition. Then, we remove duplicate structures by comparing them based on their energies and space groups, i.e., two structures with the same space group are considered distinct if the difference in their CENT energies is larger than 10^{-4} Ha.

III. RESULTS AND DISCUSSION

A. Stoichiometric structures

We carry out structure prediction simulations for the stoichiometric phases of MgO with the minima hopping method. During this search we discover metastable phases and some of their stacking faults which have been previously reported either in materials databases [58, 59] or in the literature [16, 43, 53]. The structural data of these polymorphs are presented in the Supplementary Material [60]. We enumerate these structures with labels from S01 to S25, and for each one of them we list the corresponding space-group, the number of atoms in their unit cell, the relative formation energies (ΔE_f), the volumes per Mg atom (V/V_{RS}) with respect to the ground-state RS structure, and the band-gap energies in Table I. We define the formation energy per atom,

$$E_f = (E(\text{Mg}_n\text{O}_m) - nE(\text{Mg}) - \frac{m}{2}E(\text{O}_2))/(n+m), \quad (1)$$

where $E(\text{Mg}_n\text{O}_m)$ is the total energy of the structure, and n and m are the number of magnesium and oxygen atoms, respectively. Also, $E(\text{Mg})$ is the energy of a single magnesium

atom, and $E(\text{O}_2)$ is the energy of an isolated oxygen molecule in its triplet ground state.

In addition to the well-known phases like the RS, *h*-MgO, wurtzite, and zincblende, which are the ambient ground states of many binary compounds such as ZnO and ZnS [16, 29, 61], our MH runs reveal several new low energy polymorphs with 12 and 24 atoms per unit cells (i.e. Mg_6O_6 and $\text{Mg}_{12}\text{O}_{12}$). Like in the RS structure, the Mg atoms in these phases have only octahedral bonding. In contrast, the energetically higher wurtzite and zincblende structures are composed of MgO_4 tetrahedrons which are stacked in hexagonal sequences. Therefore, unlike in some binary oxides like ZnO, octahedral bonding is the energetically preferred structural motif for MgO.

In particular, we discover two new phases of MgO, namely S02 and S03, with 24 atoms per unit cell in the energy range of 38 meV/atom, between RS and *h*-MgO. Earlier systematic structural searches for MgO bulk structures [16, 19] with unit cells up to 40 atoms seem to have missed these two phases, and, to the best of our knowledge, we are the first to report them here. Their small energy differences with respect to the RS ground state (26 and 33 meV/atom, respectively) suggests that these polymorphs are well within the synthesizability limit of oxide materials [62].

From the structural perspective, these two new polymorphs are modifications of the RS structure and are composed of MgO_6 octahedra and trigonal prisms, similar to the NiAs structure type, which are stacked on top of each other in various sequences and directions. Other structures with similar structural features, like the S10 and S05 (another well-known rocksalt-like structure [16, 59]), have higher energies. In Figure 3, we show the structures of the 7 low-energy MgO phases of MgO which are modifications of rock salt. As shown in Figure 3, S02 like RS is composed of the same octahedra with the difference that their directions or connectivities are changed twice in its unit cell. In fact, the connectivity of the octahedra is changed from edge-sharing to face-sharing where they are flipped.

The different structures that we observe in Figure 3 arise from subtle changes in the arrangements of the MgO_6 octahedra. The possible arrangements that we observe are shown schematically in Figure 4(a)–(c), in 2D and 3D representations. The octahedra in the RS structure are all edge-connected, as shown Figure 4(a). Figure 4(b) indicates that when an octahedron is flipped in the second layer then two consecutive octahedron will share a triangular face of the octahedra. In the S02 unit cell, it can be seen that this flip is happened twice. Therefore, S02 is composed of two layers of the RS with the stacking sequence *AB*. For S03, in addition to the octahedra flip, we also see trigonal prisms which have edge-sharing with the octahedra as Figure 4(c) represents. Therefore, the stacking sequence for S03 becomes *ABC*. Besides these structures, we discovered three new low energy rocksalt-like polymorphs i.e. S06, S07, and S08 which are energetically more favorable than the well-known structure S11 with symmetry *Ibam*. Figure 3 shows that S06 is similar to S02 with the identical stacking sequence *AB* of octahedra. Structures S07, S08 and S03 share the stacking sequence *ABC*, but

TABLE I. Structural data of stoichiometric phases of MgO. Column 1–3 contain the label, the phase name, and the space group, respectively. Column 4 contains the number of atoms in the unit cell of Mg_nO_n . Columns 5 and 6 contain the relative formation energy per atom with respect to the RS phase and the volume per Mg atom, respectively. The last column contains the PBE band gap.

Label	Phase	Space group	N	ΔE_f (eV/atom)	V/V_{RS}	Gap (eV)
S01	RS	$Fm\bar{3}m$ (225)	8	0.000	1.000	4.45
S02		$P\bar{3}m1$ (164)	24	0.026	1.003	4.13
S03		$R\bar{3}m$ (160)	24	0.033	1.004	3.75
S04	h -MgO	$P6_3/mmc$ (194)	8	0.038	1.183	3.26
S05		$P6_3/mmc$ (194)	24	0.040	1.006	4.03
S06		$R\bar{3}m$ (166)	24	0.051	1.006	4.15
S07	Wurtzite	$R\bar{3}m$ (160)	24	0.065	1.009	3.72
S08		$P\bar{3}m1$ (156)	12	0.065	1.009	3.72
S09		$P6_3mc$ (186)	8	0.074	1.267	3.38
S10	Stacking fault of Wurtzite	$R\bar{3}m$ (166)	32	0.076	1.009	4.12
S11		$Ibam$ (72)	32	0.076	1.233	3.07
S12		$R\bar{3}m$ (160)	12	0.087	1.273	3.43
S13	Zincblende	$Cmm2$ (35)	14	0.087	1.153	3.27
S14		$Pbcm$ (57)	24	0.088	1.256	3.02
S15		$P6_3mc$ (186)	8	0.092	1.274	3.44
S16	Stacking fault of Wurtzite	$P4_2/mnm$ (136)	8	0.094	1.326	3.36
S17		$R\bar{3}m$ (166)	12	0.100	1.011	4.13
S18		$I4/mcm$ (140)	8	0.101	1.328	2.92
S19	Zincblende	$F\bar{4}3m$ (216)	8	0.107	1.276	3.46
S20		$P6_3/mmc$ (194)	8	0.149	1.015	4.12
S21		$Pnma$ (62)	8	0.152	1.434	3.17
S22	Zincblende	$Cmc2_1$ (36)	8	0.156	1.093	3.64
S23		$I4/m$ (87)	8	0.160	1.509	3.29
S24		$I\bar{4}3m$ (217)	8	0.204	1.597	3.04
S25	Zincblende	$Fddd$ (70)	8	0.222	1.682	3.01

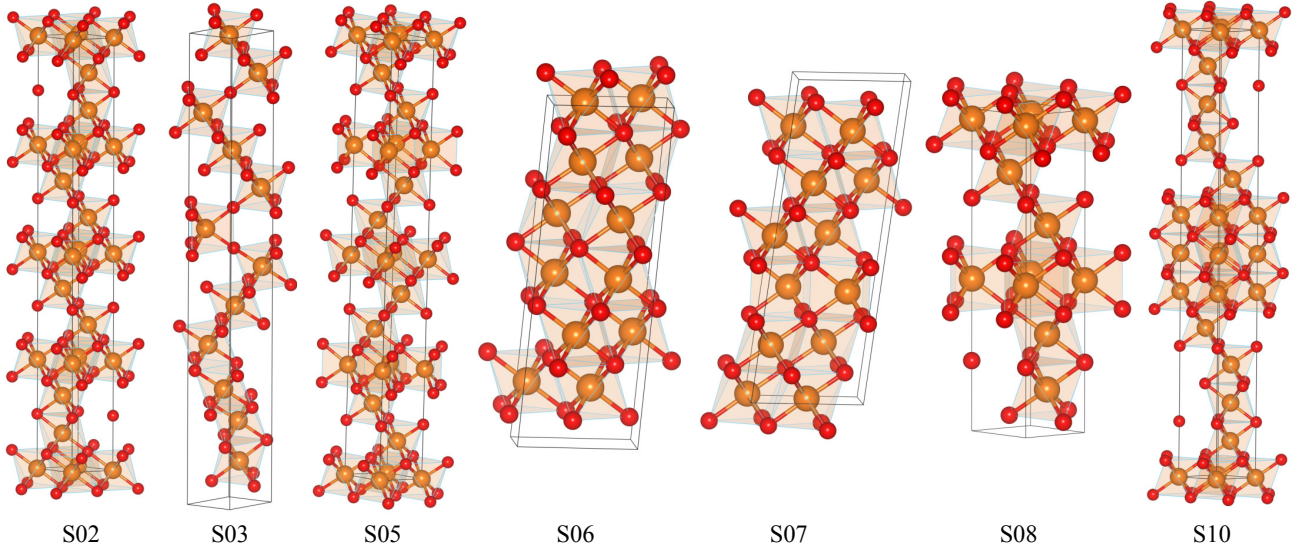


FIG. 3. The 7 low-energy modifications of the RS phase. Orange (large) and red (small) spheres denote Mg and O atoms, respectively. The structures S05 [16] and S10 [19] are reported in the literature and the others are new based on this work.

are composed of octahedra and trigonal prisms in different orderings. Also, note that the stacking periodicity for the well-known structure S05 is $ABCD$. Along the z -direction, these rocksalt-like structures are identical to RS in the $[111]$ direction.

The phonon dispersions for all the stoichiometric structures

are calculated to evaluate the dynamical stability. Supercells of dimensions $2 \times 2 \times 2$ up to $5 \times 5 \times 5$ were used depending on the unit cells. For instance, Figure 5 shows the phonon dispersion of S02. Our phonon calculations reveal that h -MgO phase (S04) is dynamically unstable at ambient conditions in agreement with earlier studies [16, 18].

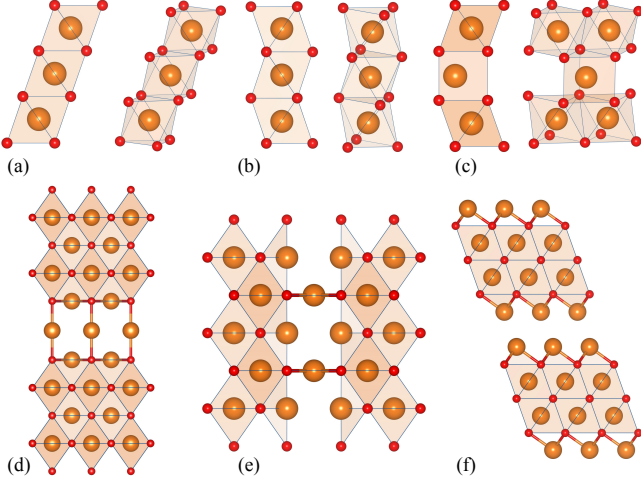


FIG. 4. (a)-(c) Motifs of the near-stoichiometric MgO structures. (d) NS3-03, (e) NS5-10, and (f) NS7-01 are three examples of the non-stoichiometric phases: (d) and (e) show the similarity in the non-stoichiometric structures in which lines of oxygen atoms are removed. (f) shows one of the GM structures in which a layer of oxygen atoms is removed.

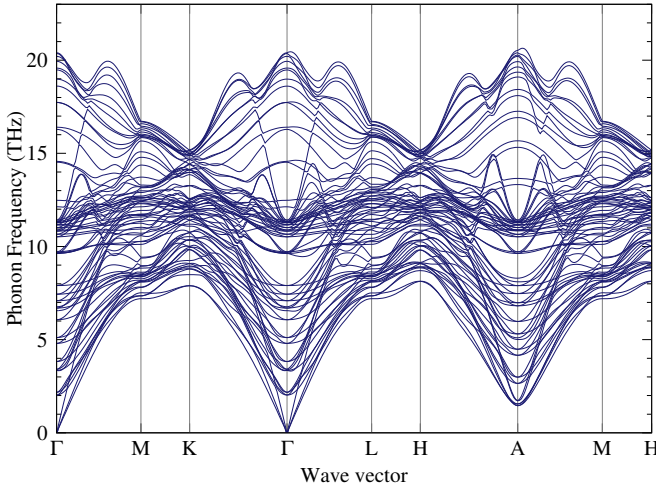


FIG. 5. The PBE phonon dispersion of S02, a new stoichiometric phase of MgO. The LO-TO splitting is neglected.

The electronic band structures of the stoichiometric phases of MgO were also calculated at the level of the PBE functional. As the results in Table I indicate, all these phases have wide band gaps. The new polymorphs S02, S03, S06, S07, and S08 which are modifications of RS with almost the same densities, have also a wide direct band gap which is however a little bit smaller than in the RS phase.

B. Structures and properties of non-stoichiometric polymorphs

In the so-called near-stoichiometric region of $\text{Mg}_x\text{O}_{1-x}$ where x varies between 0.51 and 0.57, 471 structures

where retained and validated using DFT. We find many new polymorphs with formation energies that are up to ≈ 600 meV/atom higher than the RS phase. Figure 6 shows the energetics of these novel polymorphs compared to the stoichiometric phases (Table I).

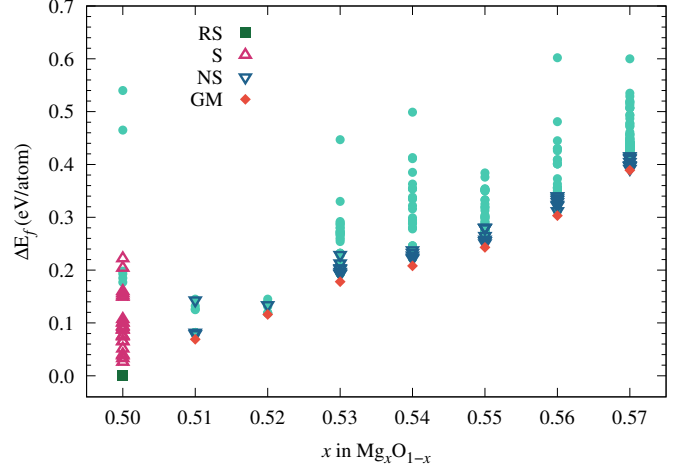


FIG. 6. The phase diagram of Mg-O near the stoichiometric region. The formation energy differences ΔE_f , calculated from Equation (1), show the distances from the convex hull as a function of x . The points S and NS represent the structures in Table I and Table II, respectively. The GM points show the global minimum structure of each composition x . The green filled circles also show all the other structures which are found in this work.

These structures are similar to each other with regard to their energies and space groups for a given composition. Hence, out of the many polymorphs that we discover for each composition, only 48 structures are selected to study their dynamical and electronic band properties in detail. (see Supplementary Material [60] for their structural data). The key properties of these non-stoichiometric structures are given in Table II.

We also compare the energy of these structures with their corresponding rock salt structures with defects for each composition of x . To this end, we first calculate the energy of an oxygen vacancy in the RS structure:

$$E_v = E_{RS}(\text{Mg}_k\text{O}_{k-1}) - E_{RS}(\text{Mg}_k\text{O}_k) + \frac{1}{2}E(\text{O}_2), \quad (2)$$

where $E_{RS}(\text{Mg}_k\text{O}_k)$ is the energy of a cubic rock salt structure with $k = 108$ and $E_{RS}(\text{Mg}_k\text{O}_{k-1})$ is the energy of the cubic rock salt with one oxygen vacancy. We can then define a reference energy for each composition in which the interaction of defects is ignored,

$$E_{ref}(\text{Mg}_n\text{O}_m) = E_{RS}(\text{Mg}_n\text{O}_n) + (n-m)E_v - \frac{(n-m)}{2}E(\text{O}_2), \quad (3)$$

where $E_{ref}(\text{Mg}_n\text{O}_m)$ is the energy of a RS structure with random oxygen defect(s) and without considering the interaction between defects. Therefore the relative defect energy per atom ΔE_d is given by,

$$\Delta E_d = (E(\text{Mg}_n\text{O}_m) - E_{ref}(\text{Mg}_n\text{O}_m)) / (n+m), \quad (4)$$

where $E(Mg_nO_m)$ is the total energy of the non-stoichiometric structures and the number of removed oxygen atoms $(n - m)$ varies between 1 to 4 in the structures. Although for some non-stoichiometric structures with a small unit cell $E_{ref}(Mg_nO_m)$ could be less accurate without the interaction effects of defects, our results (see Table II) indicate that most of the structures are more favorable than a RS structure with defects.

Note that for each composition x , we find similar configurations with different symmetries whose energies lie in a very narrow band. This indicates near-degeneracy in the non-stoichiometric structures. For example, the structure NS3-05 was selected from eight configurations with similar structural features that had however different space groups. As another example of a nearly degenerate case, we have selected the structures NS5-07–NS5-09 that have nearly identical formation energies and almost the same symmetries but different structures. Except for the structure NS3-08 which is similar to h -MgO, all the other non-stoichiometric structures are indeed similar to the RS structure. However, the values of the ratio of volume per Mg atom with respect to RS indicate that the cell does not shrink by the removal of one or several oxygen atoms but that, on contrary, it expands slightly.

These structures are formed by removing a layer of oxygen atoms located on a (111) plane or a line of oxygen atoms in the $\langle 110 \rangle$ direction in the RS structure as depicted schematically in Figure 4(d-f) for three of them. In other words, we see that the oxygen vacancies are ordered along lines or in planes.

To better understand the nature of these structures, we calculated the energy of the cubic RS structures $Mg_{216}O_{216-l}$ ($l = 2, 3$), with two or three oxygen vacancies in a perfect cell of 512 atoms. Considering all possible arrangements of the two vacancies, we found that the nearest-neighbor double vacancy along the $\langle 110 \rangle$ is the lowest in energy by 80 meV. Adding a third vacancy at various places gives the lowest energy if they are adjacent in the (111) plane. This clustering lowers the energy by 235 meV compared to configurations with large distances among the vacancies. These fairly strong interactions between vacancies explain the regular large scale patterns that we found for the non-stoichiometric structures. In fact, these results confirm the existence of oxygen-vacancy ordering, which has experimentally been observed [63–65] but to the best of our knowledge never been theoretically found by a structure prediction. It is worth mentioning that vacancy ordering can also affect the physical properties of materials such as electrical and thermal properties [66, 67]. Although we use random structures with different concentrations of oxygen vacancies as initial structures, our MH runs with the CENT potential can predict the oxygen vacancy ordering, extending in this way the power of systematic structure prediction to length scales larger than the size of a crystalline unit cell.

The dynamical stability of these structures has also been verified by phonon calculations at the DFT level. A variety of supercells were used for various unit cell sizes to verify the convergence in the phonon DOSs and force constants. The phonon calculations show that all the non-stoichiometric

structures reported in this paper are dynamically stable. Note that we neglect the Born effective charge in the phonon calculations thus the LO-TO splitting is lacking in the phonon dispersion curves. The electronic band structures and band gaps for the non-stoichiometric phases were calculated at the PBE level as indicated in Table II. In contrast to the stoichiometric polymorphs which have large gaps, the energy band gap of suboxide non-stoichiometric phases of MgO is small and 23 structures have even a pseudogap. In fact, removing O^{2-} anions results in new states in the band gap of the structures due to the extra electrons that trapped in the oxygen vacancies or the so-called F-centers [68]. This indicates that the most of the suboxide non-stoichiometric polymorphs of MgO have physical properties like semimetals or perhaps self-doped semiconductors.

As our results in Table II indicate, the GM structures of suboxide non-stoichiometric compositions i.e. NS1-01, NS2-01, NS3-01, NS4-01, NS5-01, NS6-01, and NS7-01, are similar with space groups $R\bar{3}m$ or $P\bar{3}m1$. Indeed, they are formed by ordering of the oxygen vacancies on the (111) plane of the RS phase. These structures which are indicated by the red color in Figure 6, have the same structural motifs as depicted in Figure 4(f) for NS7-01 and Figure 7(a) for NS6-01.

In the xy -plane the GM structures coincide with the RS phase and along the z -direction they are composed of rock salt (111) slabs. The top and bottom layers in these slabs are Mg atoms due to the oxygen-vacancy ordering in the (111) plane. These slabs are stacked on top of each other without any bonding between them, and only the number of atoms per primitive cell has changed for each composition x . For instance, NS6-01 has 5 magnesium atoms and 4 oxygen atoms which determine the thickness of the slabs in this structure. This is illustrated in Figure 4(f) and Figure 7(a). Although the GM structure of two compositions $x = 0.51$ and 0.53 have symmetries which are different from the others, these structures are very similar since they belong to the same point group $\bar{3}2/m$.

Our calculations demonstrate that these GM structures have a pseudogap in contrast to the large band gap of the perfect RS structure. The density of states also differs from the one of a perfect RS structure with a single vacancy. In the latter case there is a single defect level peak in the density of states whereas in the former case there is a low but uniform density of states in the original gap (see Figure 8). This small and quite uniform density of states arises from the strong dispersion of the electronic band in the original RS band gap is shown in Figure 7(c). For this polymorph, we also performed the electronic structure calculations with the hybrid functional PBE0 [69, 70]. Although hybrid functionals usually give a better description of band gap, close to the experimental values, it yields the same results as PBE for this structure. Therefore, in the GM structure of each composition the Fermi level is crossed by the electronic states which can give rise to interesting electronic properties.

The phonon dispersions of NS6-01 are illustrated in Figure 7(b) which shows dynamical stability of these structures. Note that for the phonon and electronic band structure calculations of these GM structures, we have also applied Van der

TABLE II. Structural data of non-stoichiometric phases of MgO. Column 1 contains label, followed by the space group. Columns 3–4 contain x values and number of atoms in the unit cell of Mg_nO_m , respectively. Column 5 and 6 contain the relative defect and formation energies per atom, respectively. Column 7 lists the ratio of volume per Mg atom. The last column contains the PBE band gap (* the structures with a pseudogap).

Label	Space group	x	N (n, m)	ΔE_d (eV/atom)	ΔE_f (eV/atom)	V/ V_{RS}	Gap (eV)
NS1-01	$P\bar{3}m1$ (164)	0.51	39 (20, 19)	−0.009	0.069	1.005	*
NS1-02	$Cmmm$ (65)	0.51	39 (20, 19)	0.001	0.079	1.005	1.18
NS1-03	$Immm$ (71)	0.51	39 (20, 19)	0.004	0.082	1.006	2.35
NS1-04	$R\bar{3}m$ (160)	0.51	39 (20, 19)	0.065	0.143	1.015	1.77
NS2-01	$R\bar{3}m$ (166)	0.52	46 (24, 22)	−0.016	0.116	1.009	*
NS2-02	$Cmmm$ (65)	0.52	23 (12, 11)	0.001	0.134	1.009	0.82
NS3-01	$P\bar{3}m1$ (164)	0.53	30 (16, 14)	−0.025	0.178	1.014	*
NS3-02	$C2/m$ (12)	0.53	30 (16, 14)	−0.011	0.193	1.013	0.81
NS3-03	$P4/mmm$ (123)	0.53	30 (16, 14)	−0.009	0.194	1.017	*
NS3-04	$C2/m$ (12)	0.53	30 (16, 14)	−0.006	0.197	1.016	1.14
NS3-05	$Cmmm$ (65)	0.53	30 (16, 14)	−0.001	0.202	1.013	0.53
NS3-06	$P2/c$ (13)	0.53	30 (16, 14)	0.000	0.204	1.014	1.20
NS3-07	$Fmmm$ (69)	0.53	15 (8, 7)	0.010	0.213	1.015	2.66
NS3-08	$Amm2$ (38)	0.53	15 (8, 7)	0.026	0.229	1.192	1.09
NS4-01	$R\bar{3}m$ (166)	0.54	26 (14, 12)	−0.027	0.208	1.015	*
NS4-02	$C2/m$ (12)	0.54	26 (14, 12)	−0.013	0.222	1.015	0.35
NS4-03	$I4/mmm$ (139)	0.54	13 (7, 6)	−0.010	0.224	1.019	*
NS4-04	$C2/m$ (12)	0.54	26 (14, 12)	−0.007	0.228	1.018	1.10
NS4-05	$P2/m$ (10)	0.54	26 (14, 12)	−0.002	0.233	1.015	0.16
NS4-06	$Immm$ (71)	0.54	13 (7, 6)	0.003	0.238	1.015	0.57
NS5-01	$R\bar{3}m$ (166)	0.55	22 (12, 10)	−0.035	0.243	1.019	*
NS5-02	$C2/m$ (12)	0.55	33 (18, 15)	−0.027	0.251	1.023	*
NS5-03	Cm (8)	0.55	33 (18, 15)	−0.022	0.255	1.018	*
NS5-04	$Pmm2$ (25)	0.55	33 (18, 15)	−0.022	0.255	1.020	*
NS5-05	$Pmm2$ (25)	0.55	33 (18, 15)	−0.019	0.258	1.018	0.55
NS5-06	$P4/mmm$ (123)	0.55	11 (6, 5)	−0.012	0.265	1.022	*
NS5-07	$C2/m$ (12)	0.55	11 (6, 5)	0.002	0.280	1.018	0.71
NS5-08	$P2/m$ (10)	0.55	11 (6, 5)	0.002	0.280	1.018	0.69
NS5-09	$C2/m$ (12)	0.55	11 (6, 5)	0.003	0.280	1.018	0.92
NS5-10	$Pmmm$ (47)	0.55	11 (6, 5)	0.003	0.281	1.018	0.49
NS6-01	$R\bar{3}m$ (166)	0.56	9 (5, 4)	−0.036	0.303	1.019	*
NS6-02	$Immm$ (44)	0.56	27 (15, 12)	−0.027	0.312	1.024	*
NS6-03	$P2_1/m$ (11)	0.56	18 (10, 8)	−0.017	0.322	1.021	0.68
NS6-04	$I4/mmm$ (139)	0.56	9 (5, 4)	−0.015	0.324	1.026	*
NS6-05	$C2/m$ (12)	0.56	18 (10, 8)	−0.010	0.329	1.026	0.87
NS6-06	$Immm$ (71)	0.56	27 (15, 12)	−0.006	0.333	1.026	*
NS6-07	$P2/m$ (10)	0.56	18 (10, 8)	−0.003	0.336	1.022	*
NS6-08	$C2/m$ (12)	0.56	9 (5, 4)	0.001	0.340	1.023	0.90
NS6-09	$Immm$ (71)	0.56	9 (5, 4)	0.001	0.340	1.023	0.55
NS7-01	$R\bar{3}m$ (166)	0.57	28 (16, 12)	−0.047	0.389	1.029	*
NS7-02	$P2_1/m$ (11)	0.57	28 (16, 12)	−0.044	0.392	1.029	*
NS7-03	$Pmmm$ (47)	0.57	28 (16, 12)	−0.039	0.397	1.032	*
NS7-04	$Cmmm$ (65)	0.57	28 (16, 12)	−0.039	0.397	1.031	*
NS7-05	$C2/m$ (12)	0.57	28 (16, 12)	−0.037	0.399	1.035	*
NS7-06	$Cccm$ (66)	0.57	28 (16, 12)	−0.031	0.405	1.029	*
NS7-07	$P2_1/m$ (11)	0.57	14 (8, 6)	−0.025	0.411	1.027	0.26
NS7-08	$P2_1/m$ (11)	0.57	14 (8, 6)	−0.023	0.413	1.028	0.49
NS7-09	$P4/mmm$ (123)	0.57	7 (4, 3)	−0.020	0.416	1.033	*

Waals corrections.

We also investigated the lattice thermal properties since the CENT potential can give a good and reliable description of the third-order IFCs. Although in high purity metals, the electronic part of the thermal conductivity dominates [71], we expect that due to the small amount of electrons which lie above

the pseudo gap in the GM structures, the lattice thermal conductivity should be important for these structures.

For large unit cells, assessing the lattice thermal conductivity from first principles is computationally prohibitive. We therefore resort to employ only the CENT potential to compute the anharmonic interatomic force constants. We calcu-

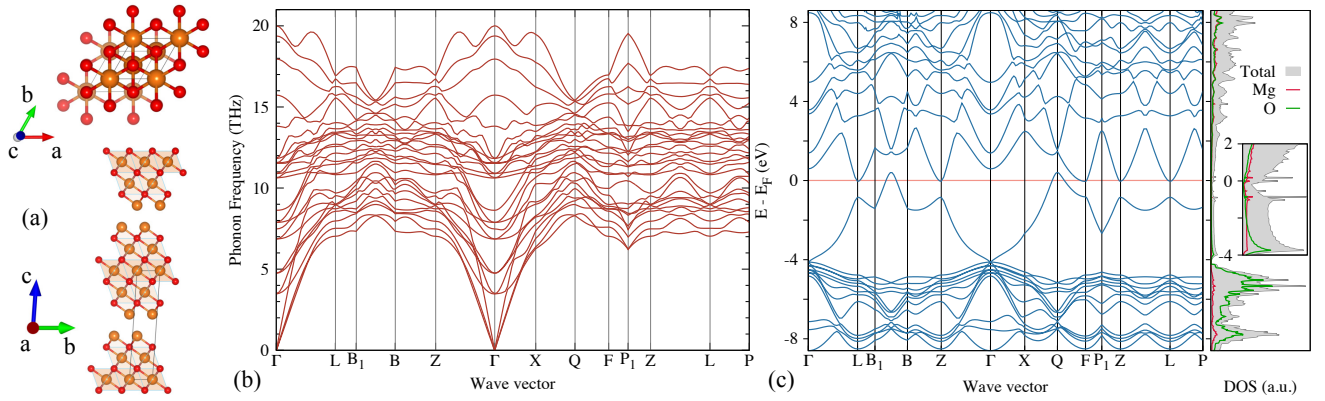


FIG. 7. (a) Crystal structure of NS6-01 viewed along the [111] direction (top) and the [100] direction (bottom) of the RS phase. (b) PBE phonon dispersion (by neglecting LO-TO splitting) and (c) PBE electronic band structure together with the total and projected density of states of the polymorph. The inset magnifies the density of states near the Fermi energy.

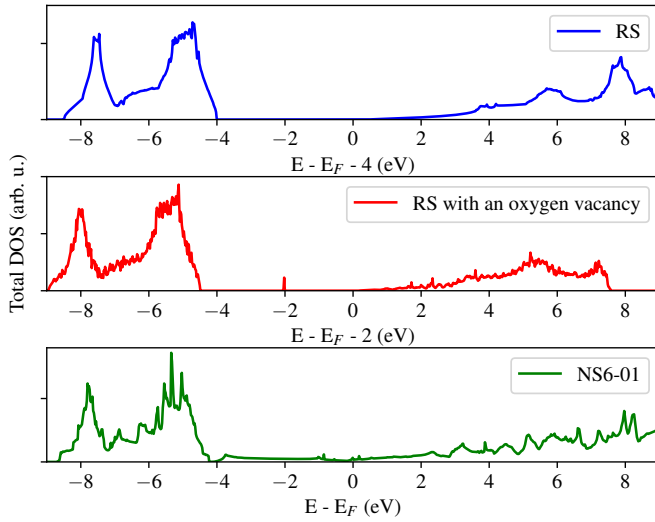


FIG. 8. Comparison of the electronic densities of states of the RS phase with and without an oxygen and of phase NS6-01. For better visibility, the Fermi energy of the first two structures are shifted by -4 and -2 eV, respectively.

late the thermal conductivity of NS6-01 using a supercell of $4 \times 4 \times 2$ including 288 atoms. We only consider atomic interactions up to the sixteenth nearest neighbors for which the lattice thermal conductivity is converged. To compute the anharmonic IFCs for this system with 9 atoms per primitive cell, the atomic forces on 4576 displaced structure are required. In addition to the supercell size and the converged cutoff value, we tested the other parameters, e.g. the number of k-points along each axis in the reciprocal space and the scale parameter for Gaussian smearing, that are necessary to obtain a converged thermal conductivity with the approach implemented in the ShengBTE code. The results are depicted in Figure 9 in which the thermal conductivities of NS6-01 along the $x-y$ plane and z -direction are compared with the RS structure. The thermal conductivity in the z -direction decreases significantly up to one order of magnitude in comparison with the RS phase. Ac-

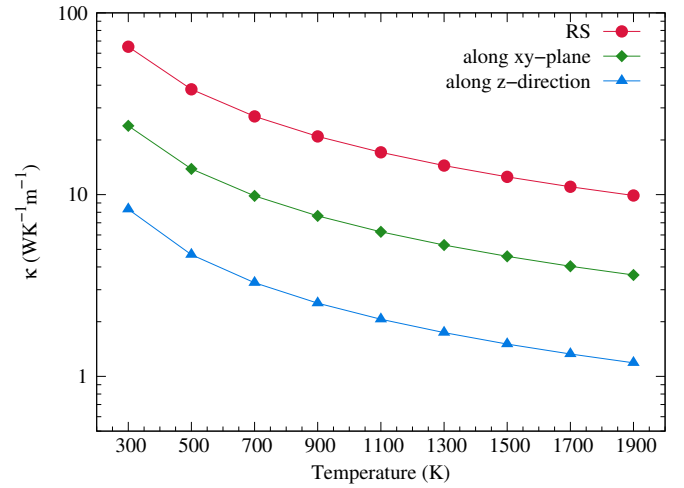


FIG. 9. Comparison of thermal conductivity of the non-stoichiometric structure NS6-01 and the RS phase.

cording to Slack's rule, the structures with a large number of atoms per primitive cell have very low values of thermal conductivity since optical modes play a key role in phonon scattering [49, 72]. On the other hand, the slabs geometry could be the other reason why only little heat is carried along the z -direction. Therefore, this amount of reduction in the thermal conductivity would not be surprising. However, such a drastic decrease in the thermal conductivity suggests that the non-stoichiometric phases of MgO could be potentially good candidates to use in several applications similar as alternatives to chemical compounds of group IV-VI elements. Also, these deviations of the electronic and thermal properties from the stoichiometric structures confirm that the GM structures of the non-stoichiometric suboxides are similar to the Magnéli-type oxides which have been reported for some materials [73, 74].

IV. CONCLUSION

We constructed a highly transferable CENT potential to explore the energy landscape of MgO compounds for both stoichiometric and non-stoichiometric compositions. This neural network potential is validated by various challenging tests such as predicting the PES of clusters and crystals of MgO as well as computing phonons and thermal transport properties. During our search, we found all the neutral $(\text{MgO})_n$ ($n = 2 - 40$) clusters and stoichiometric bulk structures of MgO which have been reported in the literature. Also, the phonon dispersion and thermal conductivity obtained for RS structures is in good agreement with the DFT results and previous theoretical and experimental works.

Subsequently, we systematically explored the phase diagram of $\text{Mg}_x\text{O}_{1-x}$ with a focus on the near-stoichiometric range. We found new low energy stoichiometric polymorphs which are modifications of the rock salt phase and studied 48 new metastable structures with non-stoichiometric compositions. We demonstrated that there is a dense spectrum of polymorphs for each composition of x ($0.51 \leq x \leq 0.57$). They all lie in a narrow energy range and are energetically more favor-

able than RS with one to four oxygen defects. This energy lowering is due to an oxygen-vacancy ordering along planes and lines.

Also, our results show that the GM structure of each composition is a structure in which the oxygen vacancies are located in (111) planes. Therefore, these structures are composed of stacked slabs of the RS structure in the direction [111] which terminate with Mg atoms. The number of layers of each slab then depends on the number of atoms in their unit cell which it increases with decreasing x . Although the GM structures have the same structural motifs, their symmetry groups are slightly different i.e. $P3m1$ for two compounds ($x = 0.51$ and 0.53) and $R3m$ for the others. They have peculiar thermal and electronic properties like Magnéli-type oxides. Thus it would be of interest to synthesize them for practical applications.

ACKNOWLEDGMENTS

The authors gratefully acknowledge support from the scientific computing core (sciCORE) facility at the University of Basel. Also, S. A. G. and H. T. thank Maximilian Amsler for valuable expert discussions and proofreading the manuscript.

-
- [1] K. Krauskopf, *Introduction to geochemistry* (McGraw-Hill, New York, 1967).
 - [2] M. Shand, *The chemistry and technology of magnesia* (Wiley-Interscience, Hoboken, N.J, 2006).
 - [3] W. MacPherson and H. Schloessin, *Physics of the Earth and Planetary Interiors* **29**, 58 (1982).
 - [4] M. Manga and R. Jeanloz, *J. Geophys. Res.* **102**, 2999 (1997).
 - [5] P. Beck, A. F. Goncharov, V. V. Struzhkin, B. Militzer, H. kwang Mao, and R. J. Hemley, *Appl. Phys. Lett.* **91**, 181914 (2007).
 - [6] T. Trevethan and A. L. Shluger, *J. Phys. Chem. C* **111**, 15375 (2007).
 - [7] W. Piskorz, F. Zasada, P. Stelmachowski, O. Diwald, A. Kortarba, and Z. Sojka, *J. Phys. Chem. C* **115**, 22451 (2011).
 - [8] G. Pacchioni and H. Freund, *Chem. Rev.* **113**, 4035 (2012).
 - [9] J. Lu, P. Serna, and B. C. Gates, *ACS Catal.* **1**, 1549 (2011).
 - [10] C. Aydin, A. Kulkarni, M. Chi, N. D. Browning, and B. C. Gates, *Angew. Chem. Int. Ed.* **52**, 5262 (2013).
 - [11] J. P. Mojica-Sánchez, T. I. Zarate-López, J. M. Flores-Álvarez, J. Reyes-Gómez, K. Pineda-Urbina, and Z. Gómez-Sandoval, *Physical Chemistry Chemical Physics* **21**, 23102 (2019).
 - [12] Y. Li, Y.-K. Peng, L. Hu, J. Zheng, D. Prabhakaran, S. Wu, T. J. Puchler, M. Li, K.-Y. Wong, R. A. Taylor, and S. C. E. Tsang, *Nature Communications* **10** (2019), 10.1038/s41467-019-12385-1.
 - [13] X. Tang and J. Dong, *Proc. Natl. Acad. Sci. U.S.A.* **107**, 4539 (2010).
 - [14] U. Schönberger and F. Aryasetiawan, *Physical Review B* **52**, 8788 (1995).
 - [15] M. A. Zwijnenburg, F. Illas, and S. T. Bromley, *Physical Review Letters* **104**, 175503 (2010).
 - [16] M. A. Zwijnenburg and S. T. Bromley, *Phys. Rev. B* **83**, 024104 (2011).
 - [17] S. Limpijumpong and W. R. L. Lambrecht, *Physical Review B* **63**, 104103 (2001).
 - [18] J. C. Schön, *Zeitschrift für anorganische und allgemeine Chemie* **630**, 2354 (2004).
 - [19] V. Stevanović, *Physical Review Letters* **116**, 075503 (2016).
 - [20] J. D. Gale, *Zeitschrift für Kristallographie - Crystalline Materials* **220**, 552 (2005).
 - [21] A. M. Ferrari and G. Pacchioni, *J. Phys. Chem.* **99**, 17010 (1995).
 - [22] G. Pacchioni, *ChemPhysChem* **4**, 1041 (2003).
 - [23] C. Roberts and R. L. Johnston, *Physical Chemistry Chemical Physics* **3**, 5024 (2001).
 - [24] T. Uchino and T. Yoko, *Physical Review B* **85**, 012407 (2012).
 - [25] S. Bhattacharya, S. V. Levchenko, L. M. Ghiringhelli, and M. Scheffler, *Physical Review Letters* **111**, 135501 (2013).
 - [26] J. Behler and M. Parrinello, *Physical Review Letters* **98**, 146401 (2007).
 - [27] S. A. Ghasemi, A. Hofstetter, S. Saha, and S. Goedecker, *Phys. Rev. B* **92**, 045131 (2015).
 - [28] S. Faraji, S. A. Ghasemi, S. Rostami, R. Rasoulkhani, B. Schaefer, S. Goedecker, and M. Amsler, *Physical Review B* **95**, 104105 (2017).
 - [29] R. Rasoulkhani, H. Tahmasbi, S. A. Ghasemi, S. Faraji, S. Rostami, and M. Amsler, *Physical Review B* **96**, 064108 (2017).
 - [30] R. Hafizi, S. A. Ghasemi, S. J. Hashemifar, and H. Akbarzadeh, *The Journal of Chemical Physics* **147**, 234306 (2017).
 - [31] S. Rostami, M. Amsler, and S. A. Ghasemi, *The Journal of Chemical Physics* **149**, 124106 (2018).
 - [32] H. Eshet, R. Z. Khaliullin, T. D. Kühne, J. Behler, and M. Parrinello, *Physical Review B* **81**, 184107 (2010).
 - [33] H. A. Eivari, S. A. Ghasemi, H. Tahmasbi, S. Rostami, S. Faraji, R. Rasoulkhani, S. Goedecker, and M. Amsler, *Chemistry of Materials* **29**, 8594 (2017).

- [34] K. Shakouri, J. Behler, J. Meyer, and G.-J. Kroes, *The Journal of Physical Chemistry Letters* **8**, 2131 (2017).
- [35] S. Faraji, S. A. Ghasemi, B. Parsaeifard, and S. Goedecker, *Physical Chemistry Chemical Physics* **21**, 16270 (2019).
- [36] M. Amsler, S. Rostami, H. Tahmasbi, E. R. Khajehpasha, S. Faraji, R. Rasoulkhani, and S. A. Ghasemi, *Comput. Phys. Commun.* **256**, 107415 (2020).
- [37] V. Blum, R. Gehrke, F. Hanke, P. Havu, V. Havu, X. Ren, K. Reuter, and M. Scheffler, *Computer Physics Communications* **180**, 2175 (2009).
- [38] J. P. Perdew, K. Burke, and M. Ernzerhof, *Phys. Rev. Lett.* **77**, 3865 (1996).
- [39] G. Kresse and J. Hafner, *Phys. Rev. B* **47**, 558 (1993).
- [40] G. Kresse and J. Hafner, *Physical Review B* **49**, 14251 (1994).
- [41] G. Kresse and J. Furthmüller, *Computational Materials Science* **6**, 15 (1996).
- [42] G. Kresse and J. Furthmüller, *Physical Review B* **54**, 11169 (1996).
- [43] M. Chen, A. R. Felmy, and D. A. Dixon, *The Journal of Physical Chemistry A* **118**, 3136 (2014).
- [44] J. Behler, *The Journal of Chemical Physics* **134**, 074106 (2011).
- [45] A. Aguado and J. M. López, *The Journal of Physical Chemistry B* **104**, 8398 (2000).
- [46] M. Haertelt, A. Fielicke, G. Meijer, K. Kwapien, M. Sierka, and J. Sauer, *Physical Chemistry Chemical Physics* **14**, 2849 (2012).
- [47] A. Togo and I. Tanaka, *Scripta Materialia* **108**, 1 (2015).
- [48] D. T. Morelli and G. A. Slack, in *High Thermal Conductivity Materials* (Springer-Verlag) pp. 37–68.
- [49] G. Slack, *Journal of Physics and Chemistry of Solids* **34**, 321 (1973).
- [50] W. Li, J. Carrete, N. A. Katcho, and N. Mingo, *Comput. Phys. Commun.* **185**, 1747 (2014).
- [51] L. Lindsay, D. A. Broido, J. Carrete, N. Mingo, and T. L. Reinecke, *Phys. Rev. B* **91**, 121202 (2015).
- [52] H. Dekura and T. Tsuchiya, *Physical Review B* **95**, 184303 (2017).
- [53] A. Schleife, F. Fuchs, J. Furthmüller, and F. Bechstedt, *Physical Review B* **73**, 245212 (2006).
- [54] S. Goedecker, *The Journal of Chemical Physics* **120**, 9911 (2004).
- [55] M. Amsler and S. Goedecker, *The Journal of Chemical Physics* **133**, 224104 (2010).
- [56] M. Sicher, S. Mohr, and S. Goedecker, *The Journal of Chemical Physics* **134**, 044106 (2011).
- [57] S. Roy, S. Goedecker, and V. Hellmann, *Physical Review E* **77**, 056707 (2008).
- [58] A. Jain, S. P. Ong, G. Hautier, W. Chen, W. D. Richards, S. Dacek, S. Cholia, D. Gunter, D. Skinner, G. Ceder, and K. a. Persson, *APL Materials* **1**, 011002 (2013).
- [59] J. E. Saal, S. Kirklin, M. Aykol, B. Meredig, and C. Wolverton, *JOM* **65**, 1501 (2013).
- [60] See Supplemental Material at [URL will be inserted by publisher] for structural data of all stoichiometric and non-stoichiometric polymorphs discussed here.
- [61] W. Sangthong, J. Limtrakul, F. Illas, and S. T. Bromley, *Phys. Chem. Chem. Phys.* **12**, 8513 (2010).
- [62] W. Sun, S. T. Dacek, S. P. Ong, G. Hautier, A. Jain, W. D. Richards, A. C. Gamst, K. A. Persson, and G. Ceder, *Sci. Adv.* **2**, e1600225 (2016).
- [63] J. F. Scott and M. Dawber, *Appl. Phys. Lett.* **76**, 3801 (2000).
- [64] S. Torbrügge, M. Reichling, A. Ishiyama, S. Morita, and Ó. Custance, *Phys. Rev. Lett.* **99**, 056101 (2007).
- [65] G. E. Murgida, V. Ferrari, M. V. Ganduglia-Pirovano, and A. M. Llois, *Phys. Rev. B* **90**, 115120 (2014).
- [66] W. Zhang, A. Thiess, P. Zalden, R. Zeller, P. H. Dederichs, J.-Y. Raty, M. Wuttig, S. Blügel, and R. Mazzarello, *Nature Mater* **11**, 952 (2012).
- [67] K. S. Siegert, F. R. L. Lange, E. R. Sittner, H. Volker, C. Schlockermann, T. Siegrist, and M. Wuttig, *Rep. Prog. Phys.* **78**, 013001 (2014).
- [68] G. Pacchioni, *The Journal of Chemical Physics* **128**, 182505 (2008).
- [69] J. P. Perdew, M. Ernzerhof, and K. Burke, *The Journal of Chemical Physics* **105**, 9982 (1996).
- [70] C. Adamo and V. Barone, *The Journal of Chemical Physics* **110**, 6158 (1999).
- [71] M. Yao, M. Zebajadi, and C. P. Opeil, *Journal of Applied Physics* **122**, 135111 (2017).
- [72] A. Eucken and G. Kuhn, *Z. Phys. Chem.* **134U**, 193 (1928).
- [73] S. Harada, K. Tanaka, and H. Inui, *Journal of Applied Physics* **108**, 083703 (2010).
- [74] G. Kieslich, U. Burkhardt, C. S. Birkel, I. Veremchuk, J. E. Douglas, M. W. Gaultois, I. Lieberwirth, R. Seshadri, G. D. Stucky, Y. Grin, and W. Tremel, *J. Mater. Chem. A* **2**, 13492 (2014).